Ocean Engineering 214 (2020) 107828

Contents lists available at ScienceDirect

Ocean Engineering

journal homepage: www.elsevier.com/locate/oceaneng

Internal waves triggered by river mouth shoals in the Yangtze River Estuary

Jianxing Wang [b], Tao Wang [c,d], Fei Xing [a], Hao Wu [b], Jianjun Jia [a], Zuosheng Yang [e], Ya Ping Wang [a,b,*]

[a] State Key Laboratory of Estuarine and Coastal Research, School of Marine Sciences, East China Normal University, Shanghai, 200241, China
[b] School of Geographic and Oceanographic Sciences, Nanjing University, Nanjing, 210093, China
[c] Key Laboratory of Marine Environment and Ecology, Ocean University of China, Qingdao, 266100, China
[d] Qingdao National Laboratory for Marine Science and Technology, Qingdao, 266100, China
[e] College of Marine Geosciences, Ocean University of China, 238 Songling Road, Qingdao, 266100, China

ARTICLE INFO

Keywords:
Internal waves
Internal hydraulics
Topography
Froude number
Mixing
Vertical transport

ABSTRACT

Internal waves are widespread in oceans and play an important role in mixing. In this study, we observed some oscillations of pycnoclines that are thought to be caused by internal waves by analyzing the vertical and temporal variations of current speed and density during ebbs of the neap tides in the south channel of the Yangtze River (Changjiang) Estuary. These oscillations have an amplitude of 1–2 m and a duration of 2–3 h. To explore the mechanism of this phenomenon, topographic features of the seabed were recorded, and a huge sandbar was observed at the place where the oscillations occurred. Therefore, we infer the oscillations in the south channel were caused by the process that the stratified water flowed over the sandbar which induced internal hydraulics and led to the excitation of internal waves. Froude number was calculated according to the internal-hydraulics equations and the results verified our hypothesis that it was the interactions between the stratified water and rapidly changing topography that triggered internal hydraulics. Internal waves caused upward-directed water movement, which influenced the vertical transport of sediment and the vertical distribution of the suspended sediment. Internal waves also increased the mass diffusivity coefficient (Kz) at the interface of internal waves.

1. Introduction

Estuaries are transition zones between rivers and oceans (Savenije, 2006). The interactions between river flow and tides are highly dynamic in estuaries due to the complex hydrologic drivers and geomorphic constraints (Du et al., 2018; Hoitink and Jay, 2016; Hoitink et al., 2017). One of the most important characteristics of estuaries is stratification. Stratification occurs when freshwater flows into saline embayment. The stratification varies temporally and spatially in different estuarine environments because of the interactions of river discharge, exchange flow, and mixing (Geyer and MacCready, 2014; MacCready et al., 2018; Wang et al., 2017). The highly stratified condition may occur due to abundant freshwater inflow and weak tidal mixing. Stratification influences the vertical mixing of the estuaries (Wang and Geyer, 2018), which greatly affects the physics and the vertical distributions of chemicals and biota. Therefore, the study of dynamic processes within stratified estuaries is crucial for understanding the estuarine dynamics and sediment transport.

Internal waves are one kind of gravity wave in stratified fluids that have attracted attention for many reasons. In the oceans, internal waves are considered to be an important driving force for mixing (Armi, 1979; Munk and Wunsch, 1998; Munk, 1966). Internal waves can cause sediment resuspension and transport in shoaling processes (Ribbe and Holloway, 2001; Southard et al., 1971; Tian et al., 2019; Wright et al., 1986), and large-scale resuspension can erode seafloor sediment and form marine nepheloid layers (Masunaga et al., 2015; Reeder et al., 2011). Internal waves can also shape the slope morphology and impact the sedimentary landscape of the seabed (Cacchione et al., 2002; Puig et al., 2004). Disturbances caused by the interactions between tidal flow and topographic features on the seabed, density stratification, and atmospheric forcing are some of the causes to excite internal waves in the oceans (Lighthill, 1978; Thorpe, 1992).

In this study, we focus our research on the south channel of the Yangtze River (Changjiang) Estuary. Yangtze River is one of the largest rivers all over the world which transports a huge amount of sediment to the ocean every year (3.68×10^8 t/yr recorded from 1951 to 2015 at the

* Corresponding author. State Key Laboratory of Estuarine and Coastal Research, School of Marine Sciences, East China Normal University, Shanghai, 200241, China.
E-mail address: ypwang@nju.edu.cn (Y.P. Wang).

https://doi.org/10.1016/j.oceaneng.2020.107828
Received 22 December 2019; Received in revised form 13 June 2020; Accepted 19 July 2020

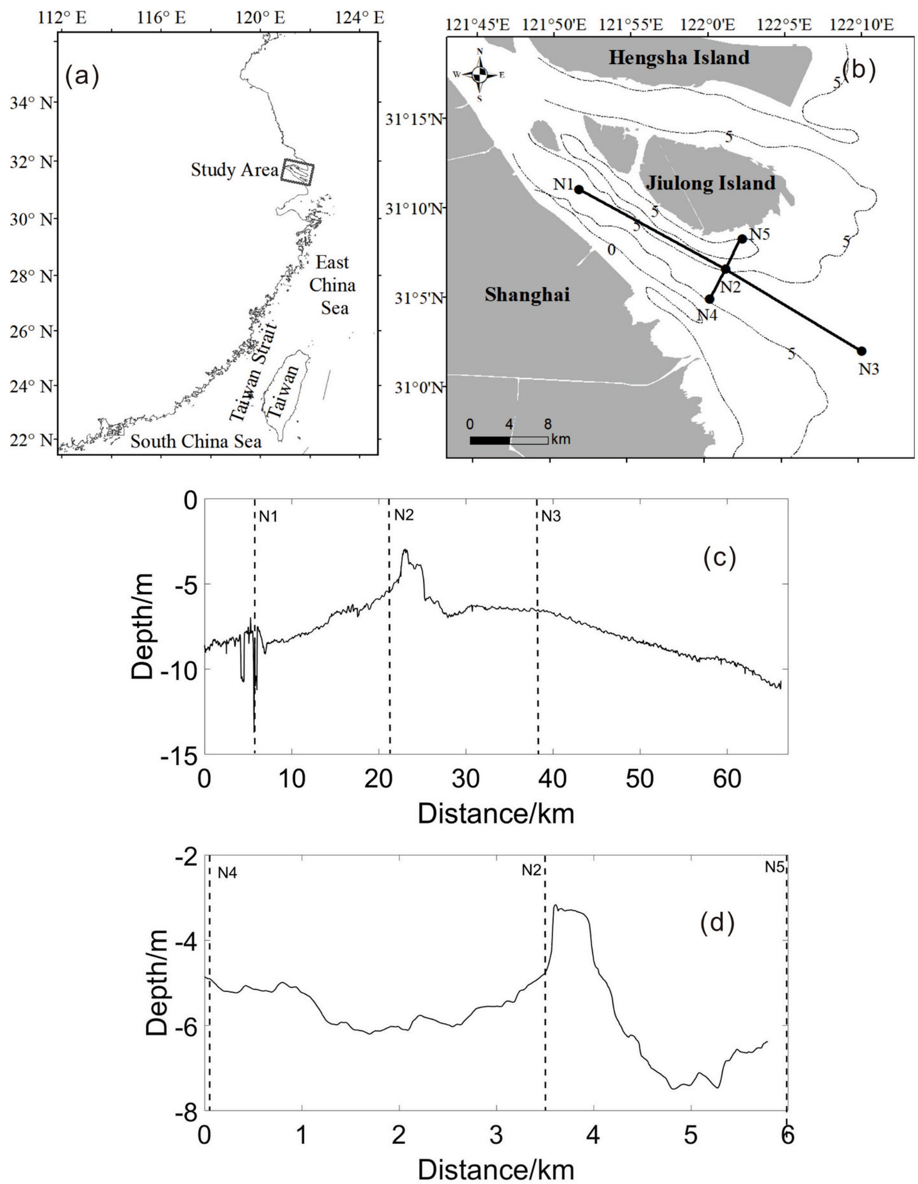

Fig. 1. Maps showing the location of the study area (a) and the southern channel of the Yangtze River Estuary (b). The black dots show the observation sites. Station N2 is the location where the sandbar was observed. Fig. 1c is the longitudinal topographic profile of the seabed from N1 to N3 and Fig. 1d is the latitudinal topographic profile of the seabed from N4 to N5.

Table 1
Detailed information about the observations, including the instruments and their deployment locations, the observed variables, and the time intervals for each instrument. One set of ADV and OBS were deployed on a bottom tripod and the others were shipboard.

Instruments	Observed variables	Location	Time Intervals
Bottom tripod			
ADV, 6 MHZ Nortek Vector	Velocity	N2 (0.25 m and 0.75 m above the seabed)	10 min intervals
OBS-3A, D&A Instrument Co.	Turbidity Temperature Salinity	N2 (0.25 m and 0.75 m above the seabed)	10 min intervals
Nortek AD2CP	Turbulence	N2 (bottom to surface)	20 min intervals
Shipboard			
TDRI ADCP, 1200 kHz	Velocity	N2 (surface to bottom; Resolution: 0.2 m)	2s intervals
Seabird-25 CTD OBS	Temperature Salinity Turbidity	N2 (surface to bottom)	Hourly (6 a.m.–0 a.m. the next day); Two hours intervals (0 a. m.–6 a.m.)
Multibeam	Topographic data	N1 to N3 N4 to N5	

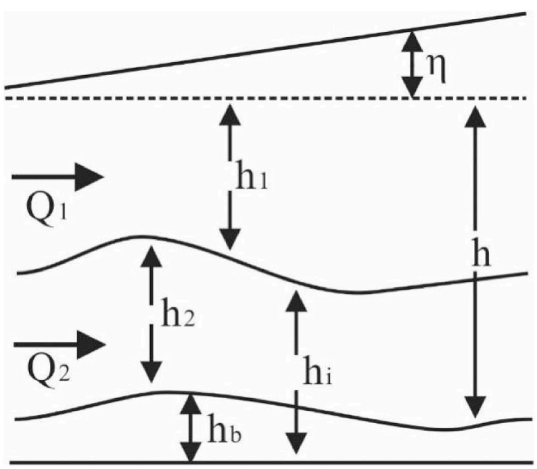

Fig. 2. Schematic of a bilayer estuary. In our study area, the longitudinal slope of η is much smaller than the slope of the bottom (h_b), so $-\partial h/\partial x$ mainly reflects the longitudinal changes of the bottom (modified from Wang et al. (2015)).

Datong Station). The south channel is one of the major channel of the estuary and a large number of ships travel cross the channel every day for fishery or transportation, so understanding the hydrodynamics in the channel is critical for the implementation of effective management. The internal waves in the Yangtze River Estuary may significantly influence the mixing and sediment transport, therefore, plays a great role in controlling the hydrodynamics and sediment transport in the estuary. We investigated the vertical structures of velocity, density, and oscillations in the south channel of the Yangtze River Estuary from December 16, 2018, to January 16, 2019, aiming at investigating whether internal waves exist in the estuary and the possible mechanisms of them. Based on the data analysis, we confirmed the existence of internal hydraulics, and the features and possible mechanisms for their excitation, as well as the impacts they brought to sediment transport in the estuary, were further discussed.

2. Study area

The Yangtze River Estuary, located near the coastal area of the East China Sea, is one of the largest estuaries all over the world (as shown in Fig. 1). The interactions between river flow and tides dominate the hydrodynamics of the Yangtze River Estuary (Cai et al., 2016). The tidal range is up to 4.6 m with its mean value of 2.7 m in the estuary. The duration of averaged ebb tides is 7.5 h, 2.5 h longer than that of averaged flood tides, indicating an irregular semidiurnal characteristic (Zhang et al., 2012). The Yangtze River discharges fluctuate following a wet-dry cycle due to the seasonal variations of precipitation in the upstream, with the maximum river discharges occurring in July and the minimum discharges occurring in January. The maximum difference in annual discharge is around 38,000 m^3/s (Cai et al., 2016). The Yangtze River bifurcates into four channels at the river mouth, among which the south channel carries most of the water and sediment discharges (56% of the total water discharge and 65% of the total sediment discharges) (Xie et al., 2015). The total length of the south channel is around 86 km and several sandbars were detected in the channel.

3. Methods

3.1. Data collection

We deployed bottom-mounted tripods at the station N2 (Fig. 1b) during the periods from December 16, 2018, to January 16, 2019, and thus, the hydrographic data were collected during both neap and spring tides were collected. One tripod was equipped with two acoustic Doppler velocimeters (ADV, 6 MHZ Nortek Vector) measuring 3-dimensional (3D) current velocities at 0.25 m and 0.75 m above the seabed. The ADV collected data in burst mode at 10 min intervals and the sampling frequency within each burst was 16 Hz, recording 8192 samples in total. Additionally, time series of turbidity, temperature, and salinity were obtained at two depths (0.25 m, 0.75 m) above the seabed using two nephelometers (OBS-3A, D&A Instrument Co.).

Apart from the near-bed tripod measurements, a boat was anchored to collect the vertical hydrodynamic and sediment data throughout the water column. Vertical velocity profiles and acoustic images from 0.8 m below the surface to depth near the seabed were obtained using a downward-looking acoustic Doppler current profiler (TDRI ADCP, 1200 kHz) every 2s with a vertical resolution of 0.2 m (each bin size). The data of vertical temperature and salinity profiles were collected for the whole water column using a Seabird-25 CTD hourly from 6 a.m. to 0 a.m. of the next day and every two hours from 0 a.m. to 6 a.m. The vertical profiles of suspended sediment concentration (SSC) were collected simultaneously with *in-situ* water-sample calibrated OBS turbidities. Turbulence dissipation rates in the water column, the rates at which turbulence kinetic energy is converted into thermal internal energy, were calculated using the data of Nortek AD2CP (16 Hz) every 20 min. We also collected topographic data by multibeam from the stations N1 to N3 and N4 to N5 (Fig. 1b), respectively. More details on the instruments we used, the observed variables, the location, and the time intervals are shown in Table 1 and Fig. 1.

3.2. Richardson number calculation

The parameterization of the condition that determines estuarine stratification is one of the most crucial aspects of estuarine dynamics. Brunt-Väisälä frequency (N^2) and Richardson number (Ri) are commonly used parameters to reflect the status of stratification and stability (Geyer and Ralston, 2011). They are expressed as:

$$N^2 = -\frac{g}{\rho}\frac{d\rho}{dz} \quad [1]$$

$$R_i = \frac{N^2}{\left(\frac{du(z)}{dz}\right)^2} \quad [2]$$

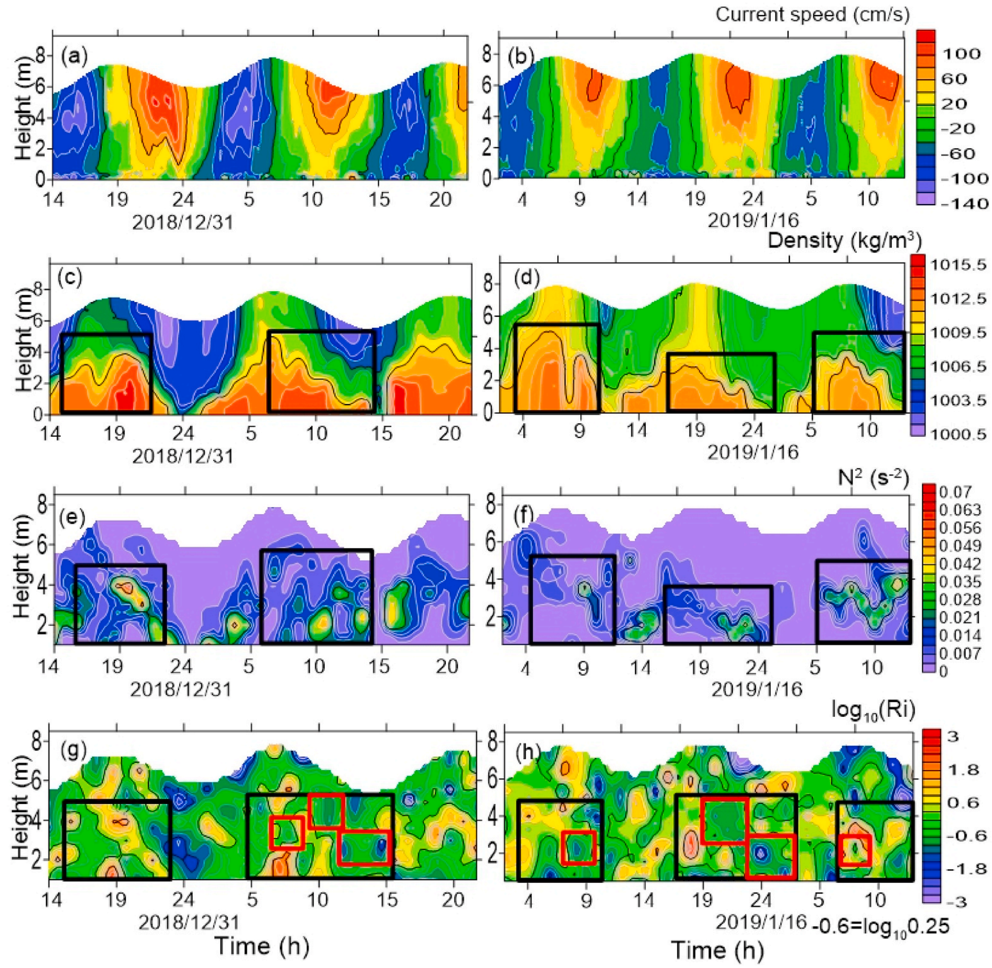

Fig. 3. Vertical distributions of current speed (cm/s), density (kg/m^3), Brunt-Väisälä frequency (N^2, s^{-2}), Richardson number ($\log_{10}$(Ri)) for December 30 to 31, 2018 (3a, 3c, 3e, 3g) and January 15 to 16, 2019 (3b, 3d, 3f, 3h). Positive velocities are seaward-directed. The black rectangles in Fig. 3c and d show the time period when the oscillations occurred and the black rectangles in Fig. 3e and f show the stratification condition of the interfaces. The black and red rectangles in Fig. 3g and h show the stability condition of the interfaces. (For interpretation of the references to colour in this figure legend, the reader is referred to the Web version of this article.)

in which u(z) is the velocity (m/s) at the depth of z (m). g is the gravitational acceleration (m/s^2) and ρ is the density of the water (kg/m^3). N^2 is an intrinsic frequency related to static stability. The frequency of the oscillation relies on the static stability: the more stratified the water column, the higher the static stability and the higher the N^2. Ri is a non-dimensional parameter used to express the trade-off between stratification and mixing. If Ri > 0.25, the stratification is strong and the velocity shear is small. If Ri < 0.25, the stratification is weak and the velocity shear is large, which is favorable to vertical mixing.

3.3. The internal-hydraulics equations

Internal hydraulic in highly stratified estuaries is typically studied by dividing the estuary into upper and lower layers separated by the pycnocline. This approach is based on the assumption that exchanges between the upper and the lower layer are slow compared to advective processes within each layer (Schijf and Schönfled, 1953; Stommel and Farmer, 1952).

Following Wang et al. (2015), a schematic of the bilayer structure is shown in Fig. 2 and the baroclinic momentum equation for the neap tide could be written as:

where $\partial h_1/\partial x$ indicates the slope of the interface, G^2 is defined as composite Froude number ($G^2 = F_1^2+F_2^2$) and z = -h_1 represents the vertical position of the interface (as shown in Fig. 2). The terms on the right-hand side (rhs) of Eq. (3) are abbreviated as a time-dependent term (TDT), a volume-dependent term (VDT), a depth-dependent term (DDT), a friction-dependent term (FDT) and a width-dependent term (WDT). TDT is correlated to the time variations of vertical velocity shear. VDT corresponds to the longitudinal variations of the volume flux of the lower layer. DDT is correlated to the bottom slope. FDT is associated with the bottom friction and WDT is caused by the longitudinal variations of the estuary.

Flow over sills in fjords is one of the practical applications of two-layer hydraulics (Geyer and Ralston, 2011). Because the slope of the seabed, $\partial h_b/\partial x$, is much larger than C_D at the station N2 (0.0045 vs. 0.0025), the bottom topography plays a more important role than friction, thus FDT is ignored in our analysis. Considering a steady flow with increasing width (like the Yangtze River Estuary), the rhs of Eq. (3) can be reduced to DDT and WDT (Geyer and Ralston, 2011). Due to the lack of data to calculate term B, we estimated the values of WDT and DDT to

$$\left(1-G^2\right)\frac{\partial h_1}{\partial x} = -\underbrace{\frac{\partial(u_1-u_2)}{g^{`}\partial t}}_{TDT} + \underbrace{\frac{1}{g^{`}B}\left(\frac{u_1}{h_1}-\frac{u_2}{h_2}\right)\frac{\partial Q_2}{\partial x}}_{VDT} - \underbrace{F_2^2\frac{\partial h}{\partial x}}_{DDT} \mp \underbrace{F_2^2 C_D}_{FDT} + \underbrace{\frac{\left(u_1^2-u_2^2\right)}{g^{`}B}\frac{\partial B}{\partial x}}_{WDT} \quad [3]$$

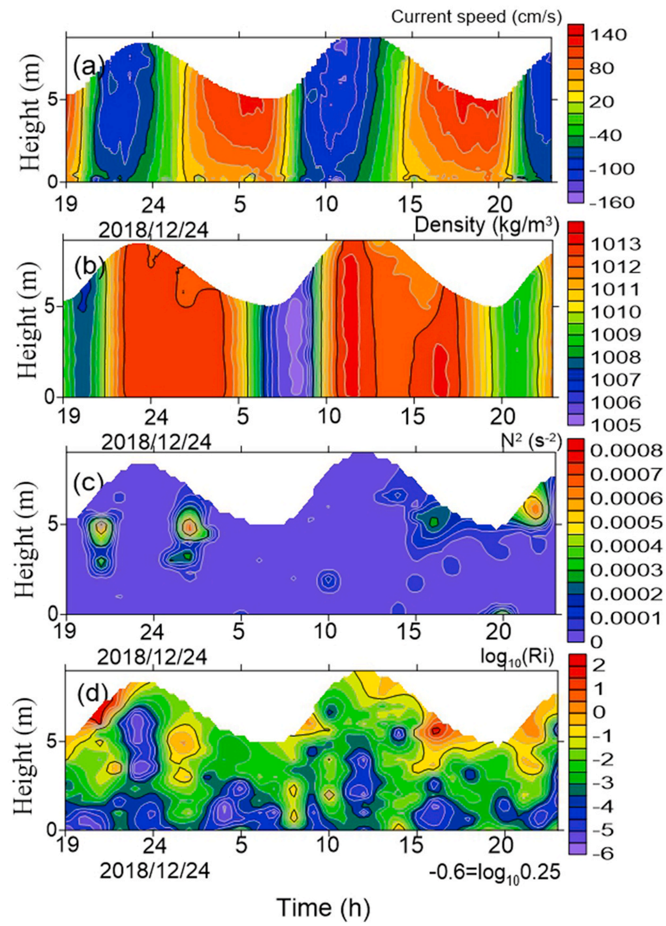

Fig. 4. Vertical distributions of current speed (cm/s), density (kg/m^3), Brunt-Väisälä frequency (N^2, s^{-2}), and Richardson number ($\log_{10}$(Ri)) from December 23 to 24, 2018 when no internal waves were detected. Positive velocities are seaward-directed.

obtain the signal of the left side of the Eq. (3) in this study. Although we have no direct evidence, it is reasonable to assume that $\partial B/\partial x$ is positive as B increases downstream along the channel.

4. Result

4.1. Topography

Topographic features on the seabed are considered to be one of the main reasons for the excitation of internal waves and huge sandbars were observed in the middle of the southern channel (as shown in Fig. 1b, c, and 1d). The steepest slope is at N2 station where the river mouth sandbar is located. The water depth above the sand bar varies from −2 m to −8 m in a longitudinal distance of ~1.3 km, so the slope $\partial h_b/\partial x$ at the station N2 is around 0.0045 (h_b is the elevation of the seabed), which is much higher compared to the averaged value of 0.0003 in the south channel. As a result, the sandbar behaves as a natural barrier for water flowing over it. The area from N1 to N2 is within the southern channel and the area from N2 to N3 is located outside of the river mouth. The water depth (h) decreases from N1 to N2 and increases from N2 to N3.

4.2. Vertical profiles of hydrodynamic properties

Two events of pycnocline oscillations occurred at N2 station during the observation (one month). The first event was on December 30 and the second was on January 15, both of which occurred during neap tides. During each event, the oscillations occurred more than one time and the correlated data were analyzed for three tidal cycles (as shown in Fig. 3). The data on December 23 and 24 when there were no oscillations were used for comparison (Fig. 4).

As shown in Fig. 3, the maximum current speeds were around 1.3 m/s and 1.4 m/s for flood tides and ebb tides, respectively, during the first period of oscillation from December 30 to 31, 2018 (Fig. 3a); and around 1.2 m/s and 1.1 m/s for flood tides and ebb tides, respectively, during the second period of oscillation from January 15 to 16, 2019 (Fig. 3b). The maximum current speeds were around 1.6 m/s and 1.4 m/s for flood tides and ebb tides from December 23 to 24, 2018 when no oscillation occurred (Fig. 4a).

The vertical density profiles, as shown in Fig. 3c, d, and 4b, were calculated based upon temperature and salinity. The vertical distributions of density varied within tidal cycles. During high water of the first period of oscillations, the density reached up to 1015.5 kg/m^3 at the bottom and was around 1006.0 kg/m^3 at the surface (as shown in Fig. 3c). For low water, the density was low throughout the entire water column (1003.0 kg/m^3 at the bottom and 1000.5 kg/m^3 at the surface) (as shown in Fig. 3c). Similarly, in the second period of oscillations, the density reached up to 1013.0 kg/m^3 at the bottom and was 1009.0 kg/m^3 at the surface for the high-water period (as shown in Fig. 3d), and the density changed to be more uniform during the low-water period (around 1006.5 kg/m^3 at the bottom and around 1005.0 kg/m^3 at the surface). From December 23 to 24, 2018, the density was vertically uniform both during the flood and the ebb. The maximum density was around 1013.0 kg/m^3 during the ebb and around 1005.0 kg/m^3 during the flood (as shown in Fig. 4b). The high-density gradient in Fig. 3c and d clearly showed the stratified condition with two different density layers divided by the pycnocline. On the other hand, the vertical uniform density profile in Fig. 4b showed a low stratified condition.

The time series of pycnoclines in Fig. 3c and d showed oscillations of the interface between the upper and the lower layers (as shown in black rectangles). No oscillations were detected in Fig. 4b. In Fig. 3c, oscillations were found during the following periods: 15:00 to 22:00 on December 30, 2018, and 6:00 to 15:00 on December 31, 2018. In Fig. 3d, oscillations were found during the following periods: 6:00 to 9:00, 19:00 to 23:00 on January 15, and 8:00 to 13:00 on January 16, 2019. These oscillations had amplitudes of 1–2 m and a duration of 2–3 h, most of which occurred during ebb tides at the intervals between the high water and the low water. As these oscillations happened close to the huge sandbar, we proposed a hypothesis that these oscillations were caused by internal hydraulics when stratified water flowed over the abruptly changing seabed (Farmer and Armi, 1999). To test this hypothesis, the Froude number was calculated using the internal-hydraulics equation (See section 4.3).

Brunt-Väisälä frequency (N^2) was calculated to show the stratification status of the water column. As shown in Fig. 3e and f, high values of N^2 (>0.02 s^{-2}) were found at the interface during the ebb tides (as shown in black rectangles). The high values of N^2 indicated highly stratified conditions at the interface. In Fig. 4c, the values of N^2 were less than 0.001 throughout the profile during the whole time period, indicating low stratification of the water column.

The impacts of the internal waves on the velocity shear (du/dz)^2 were shown in Figs. 7b, 9b and 11b. As shown in the black rectangles in Figs. 7b and 9b, the values of (du/dz)^2 increased at the interface when internal waves happened (> 0.2 s^{-2} in Fig. 7b and > 0.04 s^{-2} in Fig. 9b). On the other hand, during the time period when no internal waves were detected, Fig. 11b showed the values of (du/dz)^2 were low in the middle of the water and high at the surface and the bottom (about 0 s^{-2} in the middle of the water and > 0.05 s^{-2} at the surface and bottom). Therefore, when internal waves occurred, the significant differences in currents between the upper and lower layer caused high-velocity shear at the interface.

Richardson number (Ri) was calculated to show the stability of the water column. The $\log_{10}$(Ri) was used instead of Ri because the values of

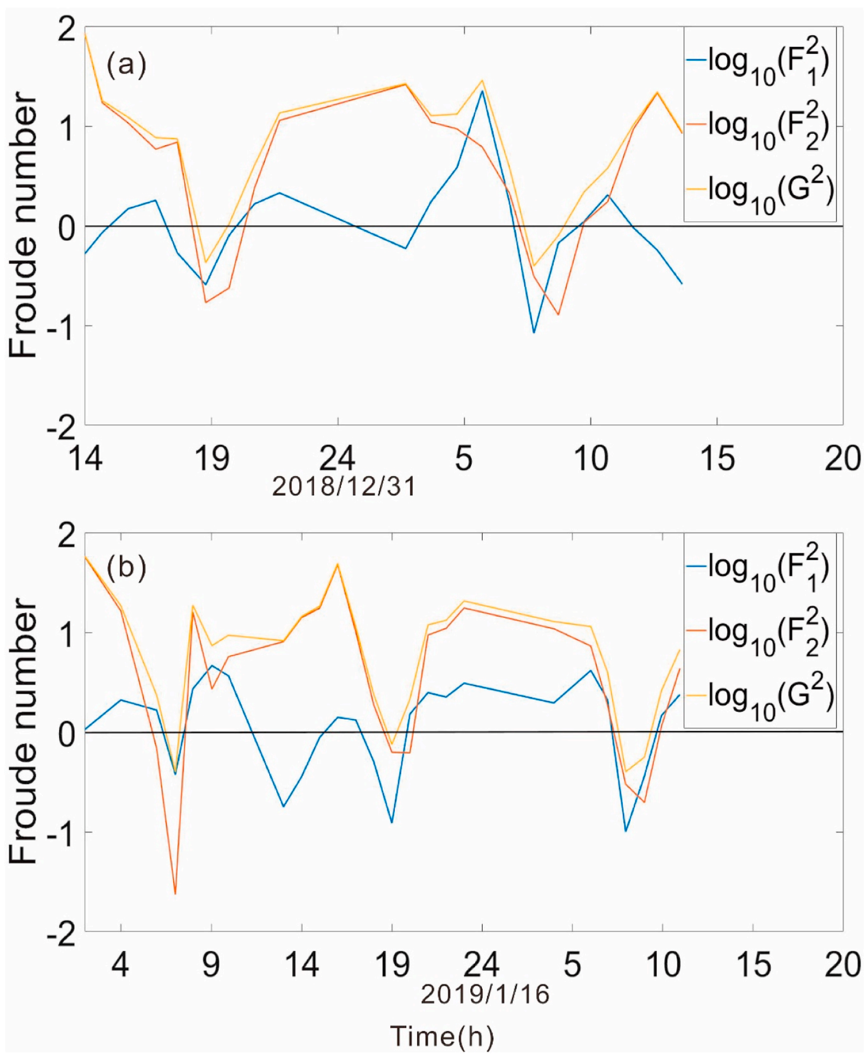

Fig. 5. Time series of Froude number ($\log_{10}(Fr)$) in two time periods. Fig. 5a is from December 30 to 31, 2018. Fig. 5b is from January 15 to 16, 2019. Internal waves were excited at the time points when the curves cross the line of 0.

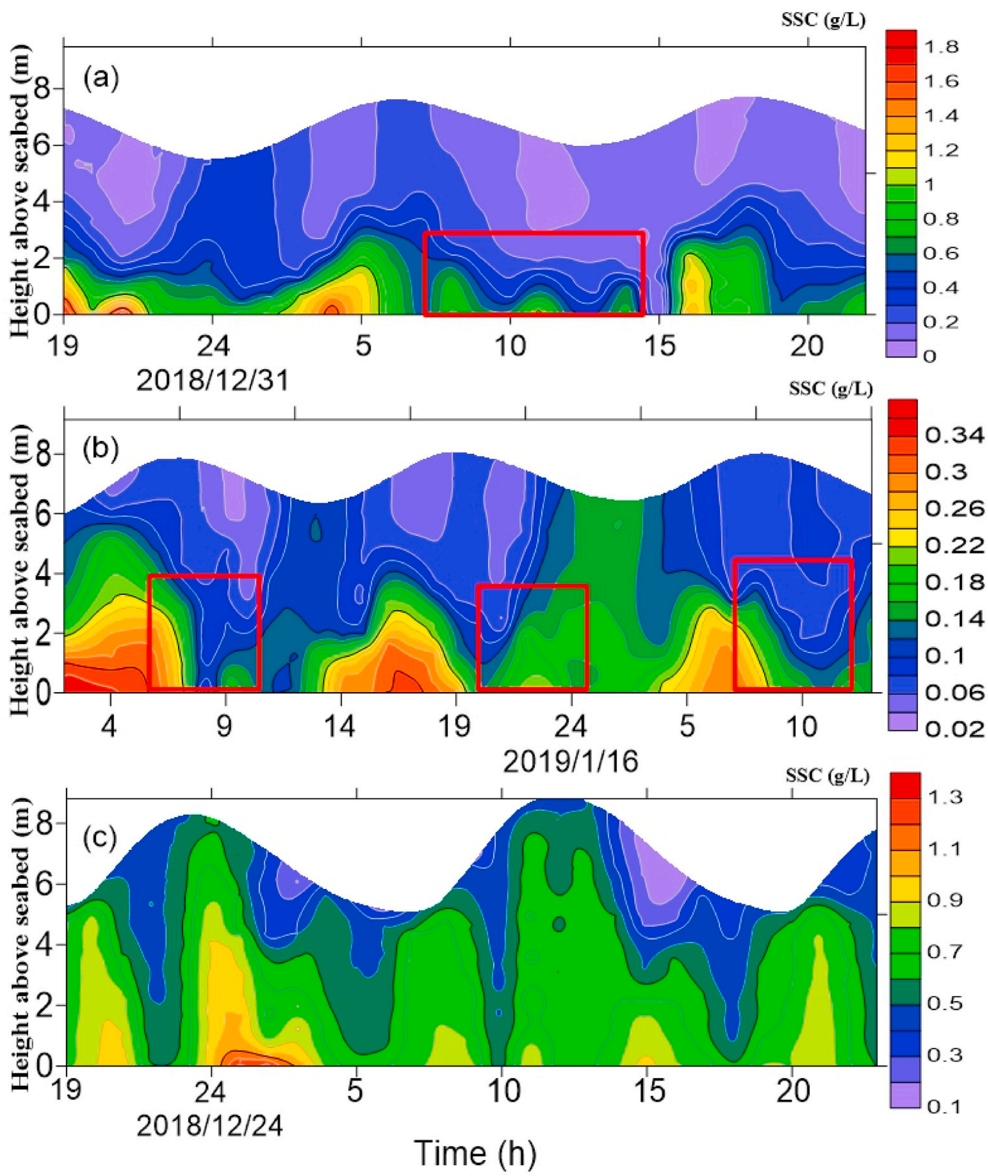

Fig. 6. Vertical distributions of observed SSC (g/L) from December 30 to 31, 2018 (a), January 15 to 16, 2019 (b), and December 23 to 24, 2018 (c). Internal waves were detected for the first two periods ((a) and (b)). The red rectangles show the oscillations influenced by internal waves. (For interpretation of the references to colour in this figure legend, the reader is referred to the Web version of this article.)

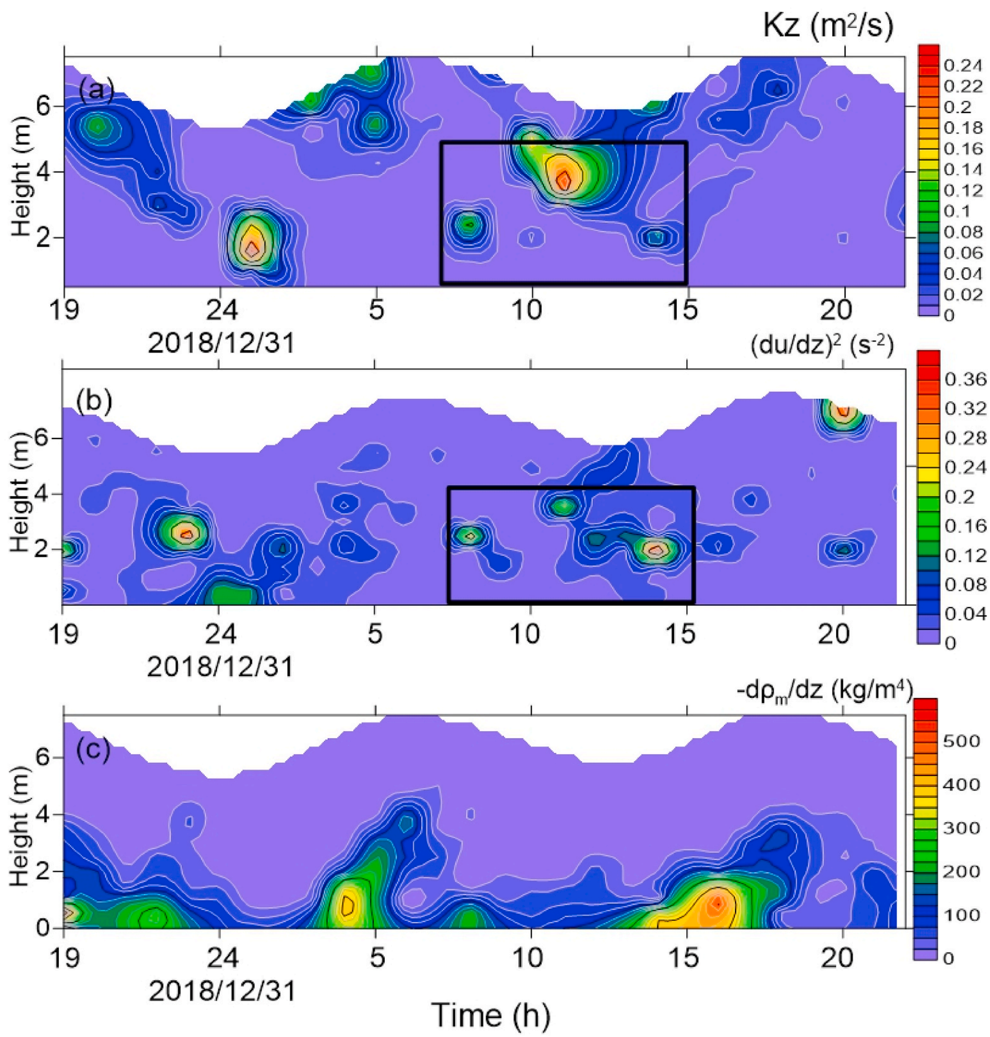

Fig. 7. Profiles of mass diffusivity coefficient (Kz, m^2/s, Fig. 7a), velocity shear squared ($(du/dz)^2$, s^{-2}, Fig. 7b) and density gradient ($-d\rho_m/dz$, kg/m^4, Fig. 7c) from December 30 to 31, 2018. Black rectangles in (a) and (b) show the increased $(du/dz)^2$ and Kz at the interface when internal waves happened.

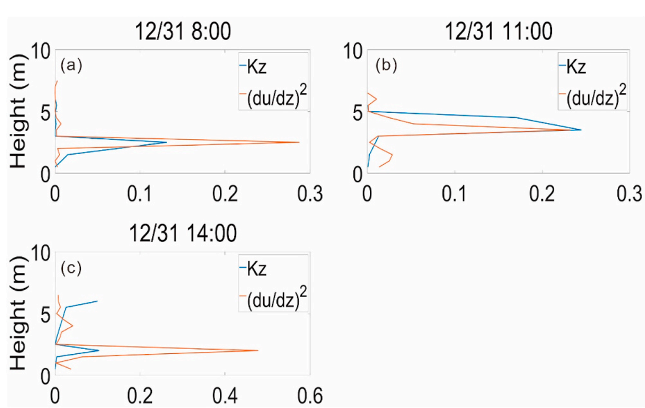

Fig. 8. Vertical distributions of the Kz (m^2/s) and $(du/dz)^2$ (s^{-2}) for the three-time points in the black rectangles of Fig. 7a and b: December 31 8:00 (a), 11:00 (b) and 14:00 (c). Kz and $(du/dz)^2$ increased at the same heights in all time points.

Ri reached very high at the interface. As shown in Fig. 3g and h, high values of $\log_{10}(Ri)$ (exceeding −0.6, which means the values of Ri to be larger than 0.25) were found at the interface, indicating the stable condition of the interface (as shown in black rectangles). However, during the time periods when internal waves happened, the values of $\log_{10}(Ri)$ dropped to around −0.6 at the interface (as shown in red rectangles in Fig. 3g and h). It indicates that internal waves weakened the stability of the water at the interface. In Fig. 4d when no internal waves were detected, the values of $\log_{10}(Ri)$ were low throughout the profile.

4.3. Mechanism of pycnocline oscillations

According to Eq. (3), the right side can be simplified to DDT and WDT. In the south channel of the Yangtze River Estuary, the width of the estuary (B) increases downstream. Water depth reduces downstream due to the sandbar. Thus, $\partial h/\partial x$ is negative and DDT is positive. Further, $\partial B/\partial x$ is positive and the average velocity of the upper layer (u_1) is either higher than the lower layer (u_2) or the same, so WDT is either positive or close to 0. Therefore, the right side WDT + DDT is always positive, indicating that the left side of the equation is positive. The left side of the equation is determined by $\partial h_1/\partial x$ and (1-G^2). G^2 is defined as composite Froude number and the term $\partial h_1/\partial x$ reflects the trend of pycnocline at the interface. When $G^2 > 1$, (1- G^2) is negative, $\partial h_1/\partial x$ should be negative. On the other hand, when $G^2 < 1$, $\partial h_1/\partial x$ is positive. When $\partial h_1/\partial x$ is negative, the pycnocline goes upwards, and vice versa. When the horizontal gradient $\partial h_1/\partial x$ varies between positive and negative values, the pycnocline fluctuates in the water column, triggering the internal

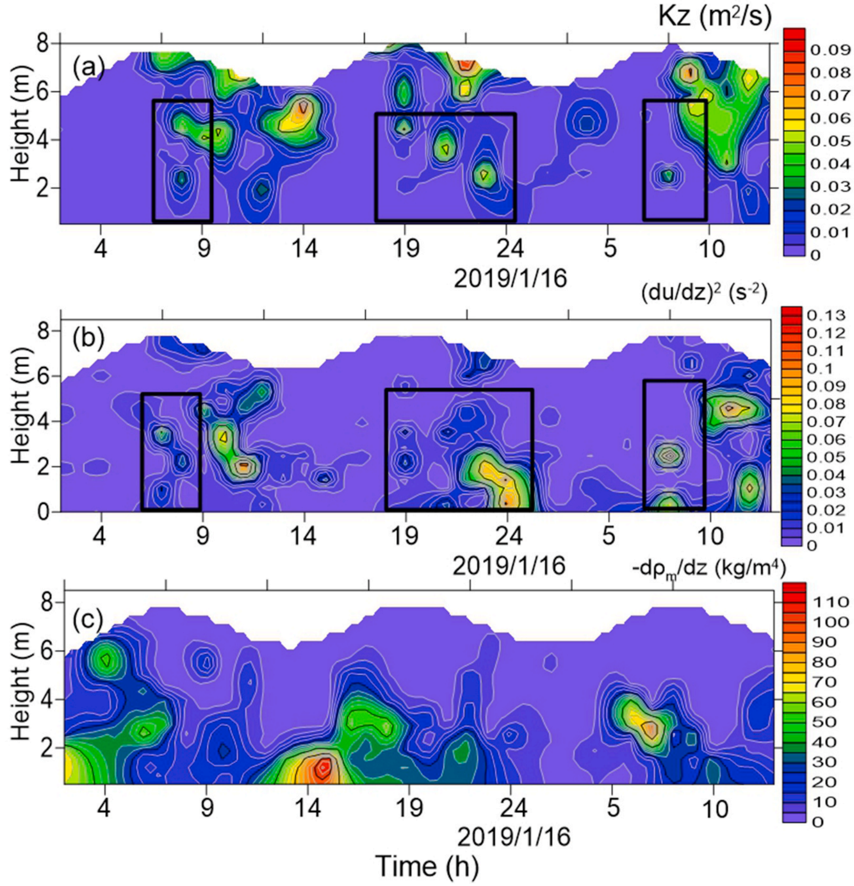

Fig. 9. Profiles of mass diffusivity coefficient (Kz, m^2/s, Fig. 9a), velocity shear squared ($(du/dz)^2$, s^{-2}, Fig. 9b) and density ($-d\rho_m/dz$, kg/m^4, Fig. 9c) from January 15 to 16, 2019. Black rectangles in (a) and (b) show the increased $(du/dz)^2$ and Kz at the interface of internal waves.

hydraulics and exciting internal waves.

By examining the variations of G^2, we can predict the occurrence of internal hydraulics. The $\log_{10}(G^2)$ is used instead of G^2 for a better presentation. From 19:00 to 20:00 on December 30, 2018, and 8:00 to 9:00 on December 31, 2018 (as shown in Fig. 5a), the values of $\log_{10}(G^2)$ were below 0, which means the values of G^2 were smaller than 1. Similarly, during the periods 7:00, 19:00 on January 15, and 8:00 to 9:00 on January 16, the calculated low values of G^2 (<1, as shown in Fig. 5b) were found. The fluctuation of the values of G^2 confirms our hypothesis that it was the stratified water flowing over the sandbar that triggered internal hydraulics and exciting internal waves. As the two events of internal hydraulics were observed within one month, it is inferred that internal waves occur occasionally in the south channel of the Yangtze River Estuary due to water stratification and the huge sandbar.

5. Discussion

Internal waves are considered to be an important driving force for mixing in oceans (Armi, 1979; Munk and Wunsch, 1998; Munk, 1966). In estuaries, internal waves are important as they also affect suspended sediment concentration (SSC) and sediment transport by influencing mixing. Besides, as sediment particles carry organic and inorganic matters, interval waves also influence the transport of organic and inorganic matters in estuaries.

The vertical SSC profiles are shown in Fig. 6a (from December 30 to 31, 2018), Fig. 6b (from January 15 to 16, 2019), and Fig. 6c (from December 23 to 24, 2018). The SSC changed within tidal cycles. In the first period of oscillations, the values of SSC reached up to 1.8 g/L at the bottom and were close to 0 g/L at the surface. During periods of high water or low water, the values of SSC were low for the entire water column (0.6 g/L at the bottom and close to 0 g/L at the surface, Fig. 6a). Similarly, in the second period of oscillation, the values of SSC reached up to 0.34 g/L at the bottom and were around 0.02 g/L at the surface (Fig. 6b), respectively. In Fig. 6c, the values of SSC reached up to 1.3 g/L at the bottom and were around 0.1 g/L at the surface. Fig. 6a and b show the highly stratified condition of the SSC and Fig. 6c indicates low stratification of the SSC.

As shown in Fig. 6c, during the period without internal waves, the variations of SSC were controlled by tidal currents and no oscillation of SSC was observed. In contrast, during the period with internal waves, the vertical SSC profiles show oscillations simultaneously (as shown in red rectangles in Fig. 6a, b, and Fig. 3c, d). The similar oscillations of SSC to that of the pycnocline indicates that the internal waves influenced the vertical distributions of the suspended sediment. When internal waves were at their crests, the oscillations of the SSC were at their crests too, and vice versa.

Mass diffusivity coefficient (Kz) is an important parameter in the dynamics of suspended sediment which shows the status of sediment diffusion. In estuarine environments, where the water is stratified, the Kz could be calculated as (Mehta, 1989; Ross, 1988):

$$\frac{Kz}{Kn} = (1 + \alpha \times \mathrm{Ri})^{-\beta} \quad [4]$$

where Kn is the neutral diffusivity. In order to account for the influences of tidal current, we use the Von Kármán expression (κ=0.408) for Kn which applies to turbulent open-channel flows (Mehta, 1989). α and β are empirical coefficients and according to Mehta (1989), $\alpha = 10$ and $\beta = 1$. Ri is the Richardson number shown in Eq. (2) but here ρ in Eq. (1) is considered the density of the water and sediment (ρ_m). ρ_m could be

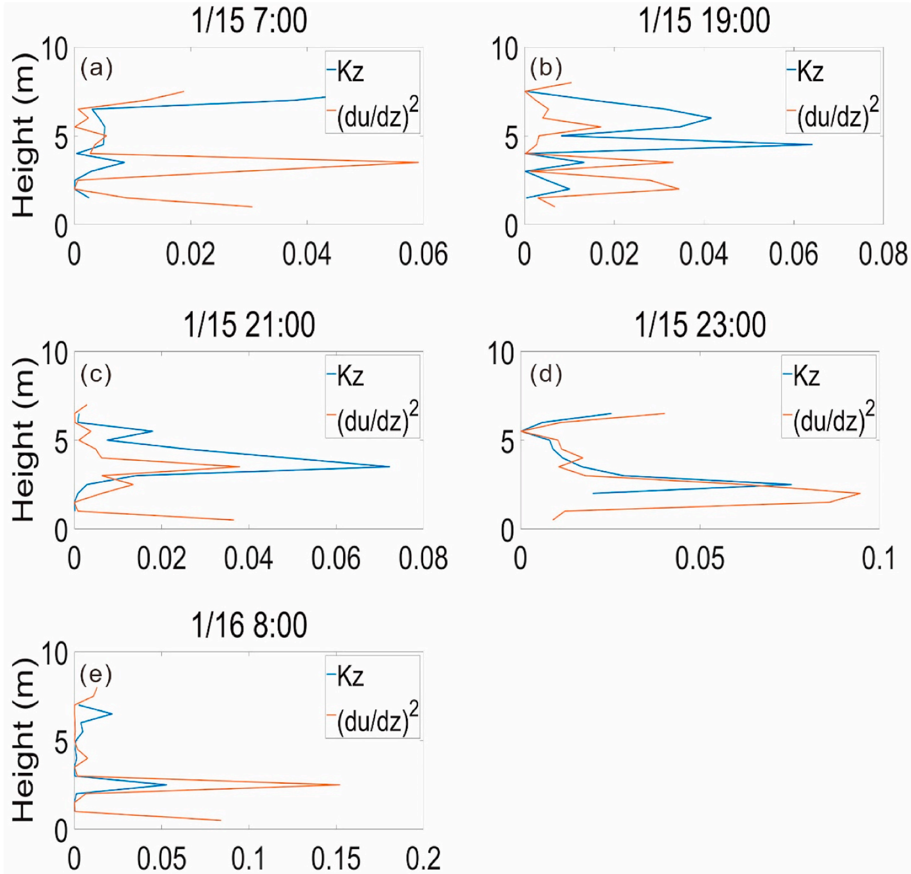

Fig. 10. Vertical distributions of the Kz (m^2/s) and $(du/dz)^2$ (s^{-2}) for five time points in the black rectangles of Fig. 9a and b: January 15 7:00 (a), 19:00 (b), 21:00 (c), 23:00 (d) and January 16 8:00 (e). Kz and $(du/dz)^2$ increased at the same heights in all time points.

calculated as (Guan et al., 2005):

$$\rho_m = C + \frac{\rho_w}{\rho_s}(\rho_s - C) \quad [5]$$

where C is the SSC (kg/m^3), ρ_w is the density of seawater (kg/m^3), ρ_s is the density of the dry sediment (=2650 kg/m^3).

We calculated the values of Kz during three time periods: December 30, 2018, January 15, 2019, and December 23, 2018. The results are shown in Figs. 7, 9 and 11. In Fig. 7, when internal waves happened on December 31 8:00, 11:00, and 14:00, the values of $(du/dz)^2$ increased at the interface, causing the values of Kz increasing at the same time (as shown in the black rectangles in Fig. 7a and b). Fig. 8 showed the vertical distributions of the Kz and $(du/dz)^2$ at these three points of time. The values of Kz and $(du/dz)^2$ increased at the same heights. Similarly, in Fig. 9, when internal waves occurred at the time points January 15 8:00, 19:00, 21:00, 23:00 and January 16 8:00, both the values of $(du/dz)^2$, and Kz increased at the interface simultaneously (as shown in black rectangles in Fig. 9a and b). Fig. 10 showed the vertical distributions of Kz and $(du/dz)^2$ at the five points of time with the same increasing trend at the interface as the other period. On the other hand, when no internal waves were detected, both the values of the $(du/dz)^2$ and Kz were low at the middle of the water (Fig. 11). In conclusion, the internal waves increased $(du/dz)^2$ at the interface, which then leads to a high mass diffusivity coefficient (Kz) simultaneously at the same location.

Vertical distributions of vertical velocity (*w*) during December 31 6:00 to 15:00, January 15 17:00 to January 16 3:00, December 23 23:00 to December 24 9:00, were analyzed and shown in Fig. 12a, b, c, respectively, to evaluate the impacts of internal waves on *w* and the vertical transport of suspended sediment. The vertical profile covered the water column from 1 m above the seabed to the water surface. The upward-directed flow was observed simultaneously with the appearance of internal waves. The upward-directed flow occurred below the interface of internal waves or throughout the whole water column (as shown in black rectangles in Fig. 12a and b), carrying sediments up. Calculations of vertical sediment transport showed that around 17.3 t and 28.8 t sediment moved upwards at 1 m height during the first period (December 31 12:00 to 14:00), and the second period (January 15 20:00 to 24:00), respectively.

The turbulence dissipation rate (ε) is the rate at which turbulence kinetic energy is converted into thermal internal energy, which is relevant to turbulence energy. The values of turbulence dissipation rate increase when internal waves break. We calculated ε with the method of Pwelch (Monin et al., 1985; Vassilicos, 2015) and the results are presented in Fig. 13. Similar trends of the turbulence dissipation rate were found during the periods with and without internal waves (Fig. 13a vs. Fig. 13b), demonstrating that the turbulence dissipation rate had no correlations with the occurrence of internal waves. It means we didn't observe the breaking of internal waves at this place. These internal waves might spread and break elsewhere.

Internal waves are widely investigated in stratified coastal oceans and have been tested to play an important role in enhancing turbulent mixing and transport of sediments and biochemically important materials (Hosegood and van Haren, 2004; Omand et al., 2011). Most internal waves are triggered by stratified water flowing over topography such as banks and sills. The observations in the south channel of the Yangtze River Estuary demonstrated that because of the sandbars at the channel, topography can be a cause of internal waves. The internal waves in the Yangtze River Estuary occurred during ebb tides between the interval of high water and low water, which was temporally consistent with former studies in estuaries (Farmer and Armi, 1999;

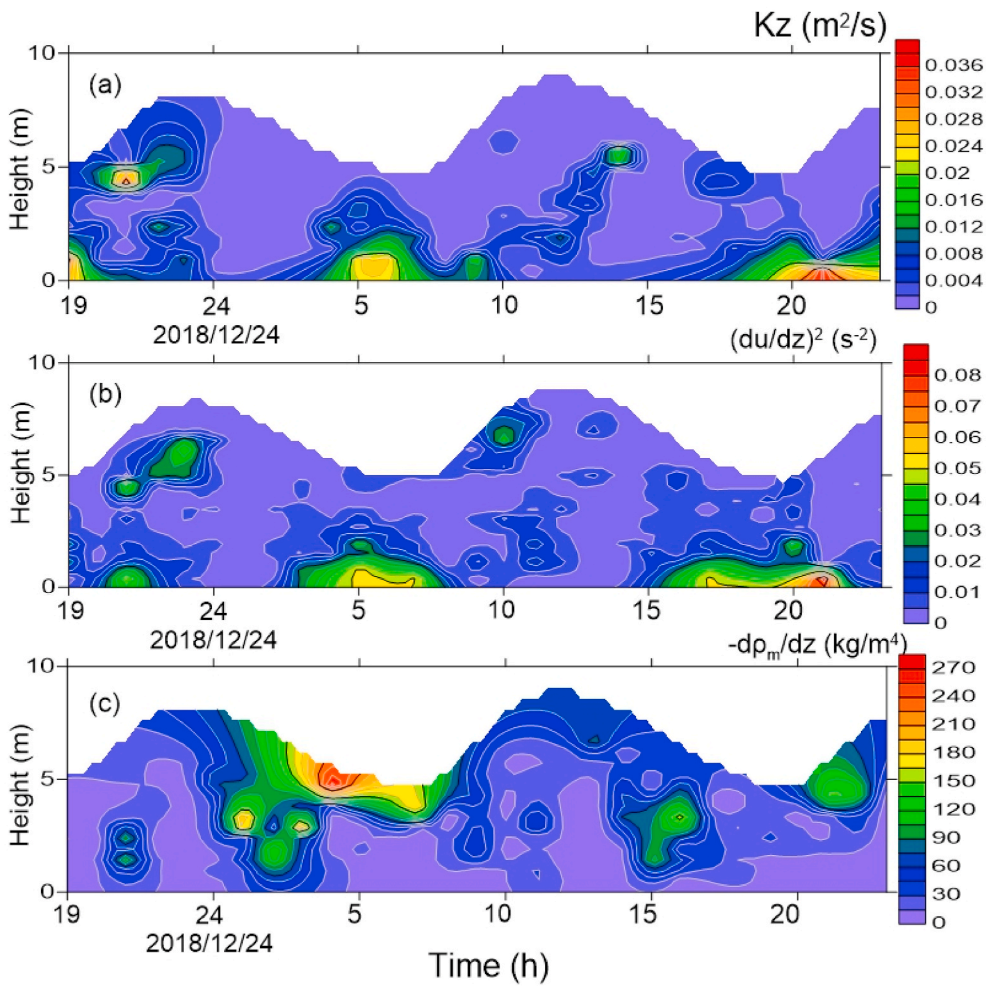

Fig. 11. Profiles of vertical diffusion modulus (Kz, m^2/s, Fig. 12a), velocity shear squared (b) ($(du/dz)^2$, s^{-2}, Fig. 12b) and density shear (c) ($-d\rho_m/dz$, kg/m^4, Fig. 12c) from December 23 to 24. The values of $(du/dz)^2$ and Kz kept low at the middle of the water column during the whole time period with a slightly increase during the high and the low water.

Geyer and Farmer, 1989; Held et al., 2019). In some other estuaries, the breaking of internal waves can weaken stratification and induce vertical mixing of sediment (Birch and Sundermeyer, 2011; Held et al., 2019; Leichter et al., 2005), leading to the diffusion of sediment into the upper water layer and significantly increased sediment transport. In this study, we didn't observe the breaking of the internal waves because the observed data were limited to one-station. Therefore, the impacts of the breaking of internal waves in the Yangtze River Estuary on the stratification and vertical mixing were not analyzed. Moreover, the important characteristics of internal waves, propagation, and the spread of these oscillations, was not observed due to the limitation of one-station data. Therefore, further researches with spatial varied dataset are needed to a deep understanding of internal waves dynamics in the Yangtze River Estuary.

6. Conclusion

Based on the analyses of the one-month observed data from December 18, 2018, to January 17, 2019, it is confirmed that internal waves existed during the ebb of neap tides at the south channel of the Yangtze River Estuary. During neap tides, the water flow became stratified and suitable for the excitation of internal waves. These internal waves were triggered by stratified water flowing over the sandbars, which created internal hydraulics. Vertical distributions of suspended sediment concentration (SSC) showed similar oscillation patterns as the internal waves, which indicates that the internal waves influenced the vertical distribution of the sediment. The results of the mass diffusivity coefficient (Kz) analysis showed that the internal waves increased Kz at the interface. Internal waves caused upward-directed flow (w), leading to the vertical transport of sediment.

Further researches on internal waves are needed as they would be affected by climate changes and human activities. Floods can intensify the stratification of water in estuaries and increase the occurrence of internal waves. Human activities such as sand-excavating in estuaries may cause internal waves to move upstream. Enclosing tideland for cultivation may also affect internal waves.

Credit author statement

The contributions made by each of the authors are listed as follows:

1. Ya Ping Wang put forward the idea and funded the study, and revised the manuscript.
2. Jianxing Wang processed the main measurements/experiments data and completed the manuscript.
3. Wang Tao put forward the idea and revised the manuscript.
4. Hao Wu helped conducting the field observations and processing data.
5. Fei Xing, Jianjun Jia and Zuoshen Yang reviewed this article and made suggestions to improve it.

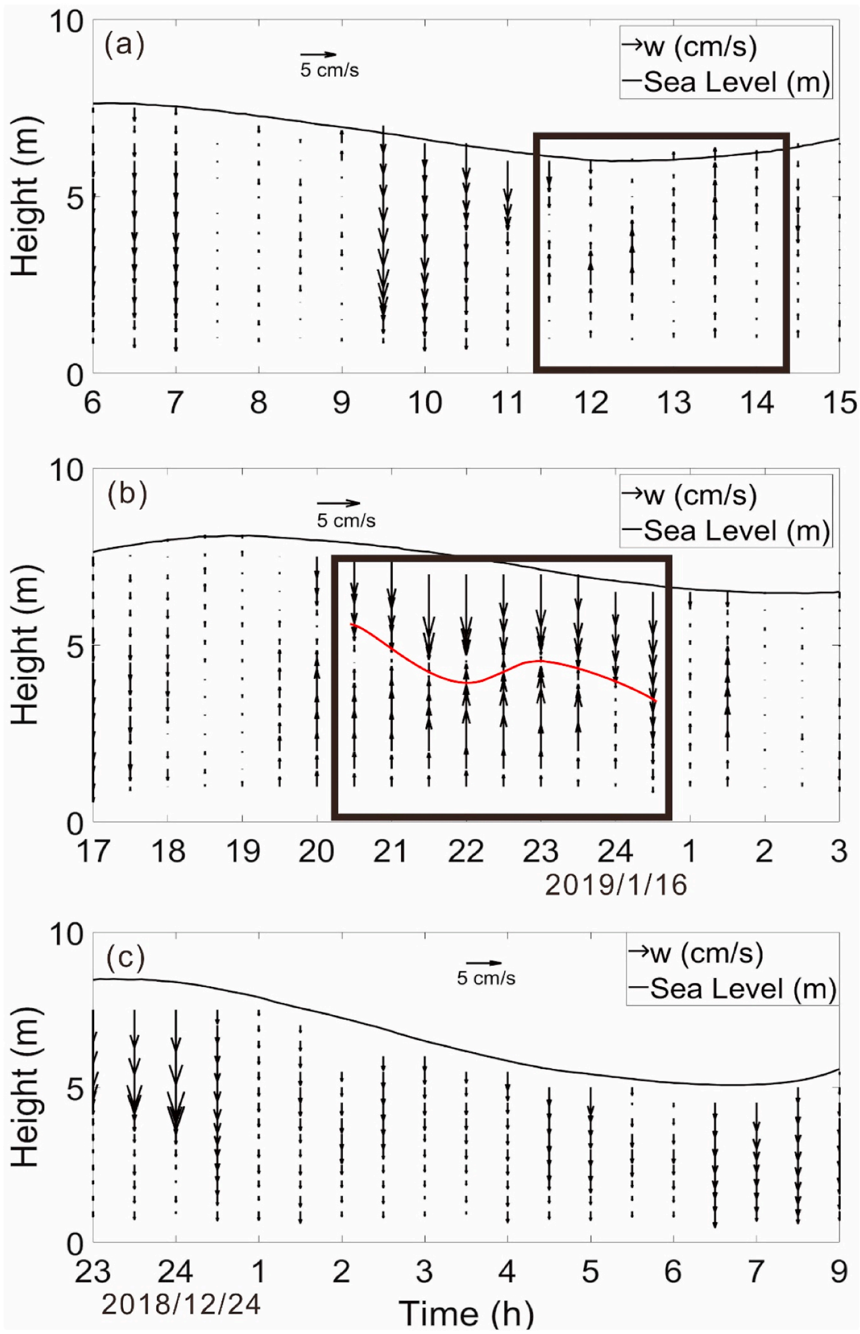

Fig. 12. Profiles of vertical velocity (*w*, cm/s) in three time periods: December 30 (a), January 15 to 16 (b) and December 23 to 24 (c). Black rectangles in (a) and (b) show the upward velocity when internal waves happened and the red curve in (b) shows the same oscillation of *w* as internal waves. (For interpretation of the references to colour in this figure legend, the reader is referred to the Web version of this article.)

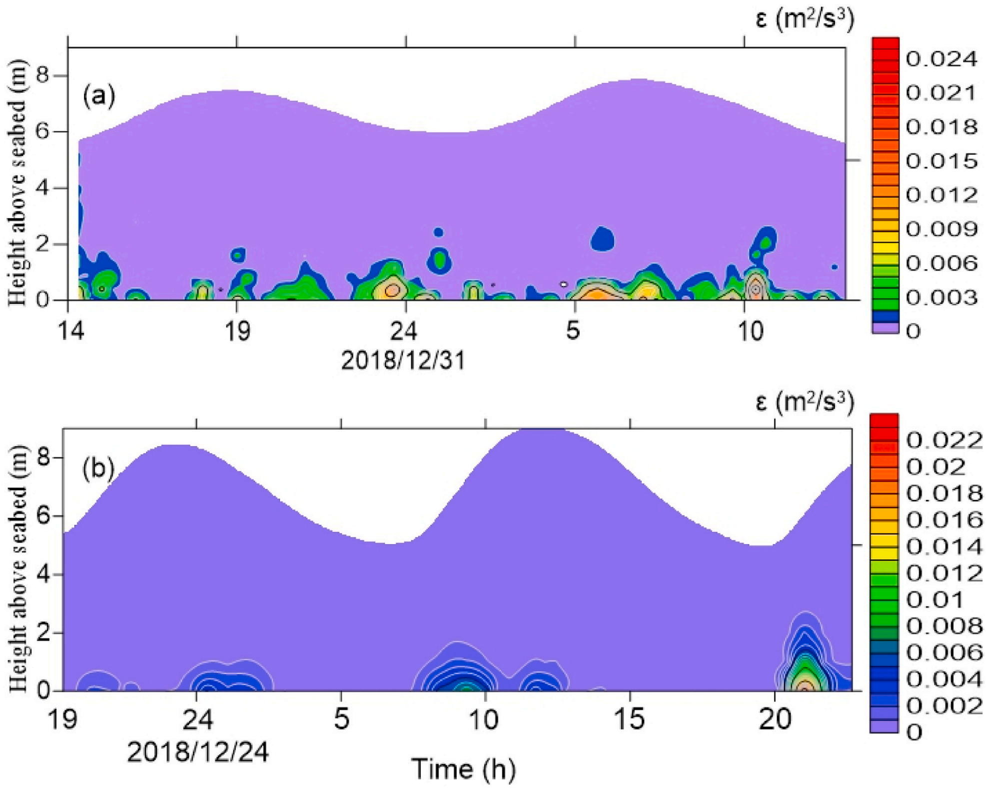

Fig. 13. Vertical distributions of turbulence dissipation rate (ε, m^2/s^3) from December 30 to 31, 2018 with internal waves (a) and December 23 to 24, 2018 without internal waves (b).

Declaration of competing interest

The authors declare that they have no known competing financial interests or personal relationships that could have appeared to influence the work reported in this paper.

Acknowledgments

We thank Lan Tingfei, Li Jiasheng, Wu Hao, Wei Dongyun, Zhao Yaqing, Cheng Gaolei, Chen Dezhi who helped in the data collection, and sediment and water samples analyses. Financial support for the study was provided by the National Natural Science Foundation of China (Nos.41625021, 41876092, 41706002) and the Innovation Program of Shanghai Municipal Education Commission (2019-01-07-00-05-E00027). JJ Jia was supported by the NSFC (No.41876092). We gratefully acknowledge constructive reviews of two anonymous reviewers.

References

Armi, L., 1979. Some evidence for boundary mixing in the deep ocean. J. Geophys. Res.-Oceans 84, 5097–5098.
Birch, D.A., Sundermeyer, M.A., 2011. Breaking internal wave groups: mixing and momentum fluxes. Phys. Fluids 23.
Cacchione, D.A., Pratson, L.F., Ogston, A.S., 2002. The shaping of continental slopes by internal tides. Science 296, 724–727.
Cai, H.Y., Savenije, H.H.G., Jiang, C.J., Zhao, L.L., Yang, Q.S., 2016. Analytical approach for determining the mean water level profile in an estuary with substantial fresh water discharge. Hydrol. Earth Syst. Sci. 20, 1177–1195.
Du, J.B., Shen, J., Zhang, Y.L.J., Ye, F., Liu, Z., Wang, Z.G., Wang, Y.P., Yu, X., Sisson, M., Wang, H.V., 2018. Tidal response to sea-level rise in different types of estuaries: the importance of length, bathymetry, and geometry. Geophys. Res. Lett. 45, 227–235.
Farmer, D., Armi, L., 1999. Stratified flow over topography: the role of small-scale entrainment and mixing in flow establishment. Proc. Math. Phys. Eng. Sci. 455, 3221–3258.
Geyer, W.R., Farmer, D.M., 1989. Tide-induced variation of the dynamics of a salt wedge estuary. J. Phys. Oceanogr. 19, 1060–1072.
Geyer, W.R., MacCready, P., 2014. The estuarine circulation. Annu. Rev. Fluid Mech. 46 46, 175–197.
Geyer, W.R., Ralston, D.K., 2011. The dynamics of strongly stratified estuaries. Treatise on Estuarine and Coastal Science 37–51.
Guan, W.B., Kot, S.C., Wolanski, E., 2005. 3-D fluid-mud dynamics in the Jiaojiang Estuary, China. Estuar. Coast Shelf Sci. 65, 747–762.
Held, P., Bartholoma-Schrottke, K., Bartholoma, A., 2019. Indications for the transition of Kelvin-Helmholtz instabilities into propagating internal waves in a high turbid estuary and their effect on the stratification stability. Geo Mar. Lett. 39, 149–159.
Hoitink, A.J.F., Jay, D.A., 2016. Tidal river dynamics: implications for deltas. Rev. Geophys. 54, 240–272.
Hoitink, A.J.F., Wang, Z.B., Vermeulen, B., Huismans, Y., Kastner, K., 2017. Tidal controls on river delta morphology. Nat. Geosci. 10, 637–645.
Hosegood, P., van Haren, H., 2004. Near-bed solibores over the continental slope in the Faeroe-Shetland Channel. Deep-Sea Res. Part II Top. Stud. Oceanogr. 51, 2943–2971.
Leichter, J.J., Deane, G.B., Stokes, M.D., 2005. Spatial and temporal variability of internal wave forcing on a coral reef. J. Phys. Oceanogr. 35, 1945–1962.
Lighthill, J., 1978. Waves in Fluids. Press, Cambridge.
MacCready, P., Geyer, W.R., Burchard, H., 2018. Estuarine exchange flow is related to mixing through the salinity variance budget. J. Phys. Oceanogr. 48, 1375–1384.
Masunaga, E., Homma, H., Yamazaki, H., Fringer, O.B., Nagai, T., Kitade, Y., Okayasu, A., 2015. Mixing and sediment resuspension associated with internal bores in a shallow bay. Continent. Shelf Res. 110, 85–99.
Mehta, A.J., 1989. On estuarine cohesive sediment suspension behavior. J. Geophys. Res.-Oceans 94, 14303–14314.
Monin, A.S., Ozmidov, R.V., Usina, L., Tennekes, H., 1985. Turbulence in the Ocean. Springer.
Munk, W., Wunsch, C., 1998. Abyssal recipes II: energetics of tidal and wind mixing. Deep-Sea Res. Part I Oceanogr. Res. Pap. 45, 1977–2010.
Munk, W.H., 1966. Abyssal Recipes, Deep Sea Research and Oceanographic Abstracts. Elsevier, pp. 707–730.
Omand, M.M., Leichter, J.J., Franks, P.J.S., Guza, R.T., Lucas, A.J., Feddersen, F., 2011. Physical and biological processes underlying the sudden surface appearance of a red tide in the nearshore. Limnol. Oceanogr. 56, 787–801.
Puig, P., Palanques, A., Guillen, J., El Khatab, M., 2004. Role of internal waves in the generation of nepheloid layers on the northwestern Alboran slope: implications for continental margin shaping. J. Geophys. Res.-Oceans 109.
Reeder, D.B., Ma, B.B., Yang, Y.J., 2011. Very large subaqueous sand dunes on the upper continental slope in the South China Sea generated by episodic, shoaling deep-water internal solitary waves. Mar. Geol. 279, 12–18.
Ribbe, J., Holloway, P.E., 2001. A model of suspended sediment transport by internal tides. Continent. Shelf Res. 21, 395–422.
Ross, M.A., 1988. Vertical Structure of Estuarine Fine Sediment Suspensions. Ph.D thesis, Univ. of Fla., Gainesville.
Savenije, H.H., 2006. Salinity and Tides in Alluvial Estuaries. Elsevier.

Schijf, J., Schönfled, J., 1953. Theoretical considerations on the motion of salt and fresh water. In: IAHR.
Southard, J.B., Cacchion, D.A., Flood, R.D., 1971. Experiments on bottom sediment movement by breaking internal waves. Trans. Am. Geophys. Union 52, 258-&.
Stommel, H.M., Farmer, H.G., 1952. On the Nature of Estuarine Circulation. Woods Hole Oceanographic Institution.
Thorpe, S.A., 1992. The generation of internal waves by flow over the rough topography of a continental-slope. Proc. R. Soc. London, Ser. A Math. Phys. Eng. Sci. 439, 115–130.
Tian, Z.C., Guo, X.J., Qiao, L.Z., Jia, Y.G., Yu, L., 2019. Experimental investigation of slope sediment resuspension characteristics and influencing factors beneath the internal solitary wave-breaking process. Bull. Eng. Geol. Environ. 78, 959–967.
Vassilicos, J.C., 2015. Dissipation in turbulent flows. Annu. Rev. Fluid Mech. 47 (1), 95–114.
Wang, T., Geyer, W.R., 2018. The balance of salinity variance in a partially stratified estuary: implications for exchange flow, mixing, and stratification. J. Phys. Oceanogr. 48, 2887–2899.
Wang, T., Geyer, W.R., Engel, P., Jiang, W., Feng, S., 2015. Mechanisms of tidal oscillatory salt transport in a partially stratified estuary. J. Phys. Oceanogr. 45, 2773–2789.
Wang, T., Geyer, W.R., MacCready, P., 2017. Total exchange flow, entrainment, and diffusive salt flux in estuaries. J. Phys. Oceanogr. 47, 1205–1220.
Wright, L., Yang, Z.-S., Bornhold, B., Keller, G., Prior, D.B., Wiseman, W., Fan, Y., Su, Z., 1986. Short period internal waves over the Huanghe (Yellow River) delta front. Geo Mar. Lett. 6, 115–120.
Xie, H., Dai, Z., Zuo, S., 2015. Morph dynamic processes of the south passage of the Yangtze Estuary (1959–2013). Ocean Eng. 33, 51–59.
Zhang, E., Savenije, H., Chen, S., Mao, X., 2012. An analytical solution for tidal propagation in the Yangtze Estuary, China. Hydrol. Earth Syst. Sci. 16.